

Applying multimodal learning to Classify transient Detections Early (AppleCiDer) I: Data set, methods, and infrastructure

ALEXANDRA JUNELL,^{1,2} ARGYRO SASLI,^{1,2} FELIPE FONTINELE NUNES,^{1,2} MAOJIE XU,^{3,2} BENNY BORDER,^{1,2} NABEEL REHEMTULLA,^{4,5,6} MARIIA RIZHKO,⁷ YU-JING QIN,⁸ THEOPHILE JEGOU DU LAZ,^{9,2} ANTOINE LE CALLOCH,^{1,2} SUSHANT SHARMA CHAUDHARY,^{1,2} SHAOWEI WU,¹ JESPER SOLLERMAN,¹⁰ NIHARIKA SRAVAN,¹¹ STEVEN L. GROOM,¹² DAVID HALE,¹³ MANSI M. KASLIWAL,¹⁴ JOSIAH PURDUM,¹⁵ AVERY WOLD,¹² MATTHEW J. GRAHAM,^{15,2} AND MICHAEL W. COUGHLIN^{1,2}

¹*School of Physics and Astronomy, University of Minnesota, Minneapolis, MN 55455, USA*

²*NSF Institute on Accelerated AI Algorithms for Data-Driven Discovery (A3D3)*

³*Department of Computer Science & Engineering, University of Minnesota, Minneapolis, MN 55455, USA*

⁴*Department of Physics and Astronomy, Northwestern University, 2145 Sheridan Road, Evanston, IL 60208, USA*

⁵*Center for Interdisciplinary Exploration and Research in Astrophysics (CIERA), 1800 Sherman Ave., Evanston, IL 60201, USA*

⁶*NSF-Simons AI Institute for the Sky (SkAI), 172 E. Chestnut St., Chicago, IL 60611, USA*

⁷*University of California, Berkeley, Department of Astronomy, Berkeley, CA, USA*

⁸*Division of Physics, Mathematics and Astronomy, California Institute of Technology, 1200 E California Blvd., Pasadena, CA 91125, USA*

⁹*Division of Physics, Mathematics, and Astronomy, California Institute of Technology, Pasadena, CA 91125, USA*

¹⁰*Department of Astronomy, Stockholm University, 10691 Stockholm, Sweden*

¹¹*Department of Physics, Drexel University, Philadelphia, PA 19104, USA*

¹²*IPAC, California Institute of Technology, 1200 E. California Blvd, Pasadena, CA 91125, USA*

¹³*Caltech Optical Observatories, California Institute of Technology, Pasadena, CA 91125*

¹⁴*California Institute of Technology, 1200 E. California Boulevard, Pasadena, CA 91125, USA*

¹⁵*Cahill Center for Astrophysics, California Institute of Technology, Pasadena, CA, 91125, USA*

ABSTRACT

Modern time-domain surveys like the Zwicky Transient Facility (ZTF) and the Legacy Survey of Space and Time (LSST) generate hundreds of thousands to millions of alerts, demanding automatic, unified classification of transients and variable stars for efficient follow-up. We present **AppleCiDer** (Applying Multimodal Learning to Classify Transient Detections Early), a novel framework that integrates four key data modalities (photometry, image cutouts, metadata, and spectra) to overcome limitations of single-modality classification approaches. Our architecture introduces *(i)* two transformer encoders for photometry, *(ii)* a multimodal convolutional neural network (CNN) with domain-specialized metadata towers and Mixture-of-Experts fusion for combining metadata and images, and *(iii)* a CNN for spectra classification. Training on $\sim 30,000$ real ZTF alerts, **AppleCiDer** achieves high accuracy, allowing early identification and suggesting follow-up for rare transient spectra. The system provides the first unified framework for both transient and variable star classification using real observational data, with seamless integration into brokering pipelines, demonstrating readiness for the LSST era.

Keywords: Time domain astronomy — Astro informatics — Classification

1. INTRODUCTION

Large-scale surveys in modern astronomy prioritize automated detection (Rebbapragada et al. 2008), which demands innovative approaches to handle the unprecedented volume and variety of astronomical data (Zhang & Zhao 2015; Poudel et al. 2022). A wide range of multi-

Corresponding author: Alexandra Junell
ajunell@umn.edu

Corresponding author: Argyro Sasli
asasli@umn.edu

wavelength facilities – such as the Neil Gehrels Swift Observatory (Swift; Gehrels et al. 2004), the Palomar Transient Factory (Law et al. 2009), Advanced LIGO (Collaboration et al. 2015), Catalina Real-Time Transient Survey (Drake et al. 2012), Asteroid Terrestrial-impact Last Alert System (Tonry et al. 2018), the Zwicky Transient Facility (ZTF; Bellm et al. 2019; Graham et al. 2019; Masci et al. 2019; Dekany et al. 2020), Einstein Probe (Yuan et al. 2022), Nancy Grace Roman Space Telescope (Mosby et al. 2020), Ultraviolet Transient Astronomy Satellite (Shvartzvald et al. 2024), Vera C. Rubin Observatory’s Legacy Survey of Space and Time (LSST; Ivezić et al. 2019), Ultraviolet Explorer (Kulkarni et al. 2023), and future Laser Interferometer Space Antenna (Amaro-Seoane et al. 2023) – offers opportunities to detect events across multiple detectors and wavelengths. However, enabling Multi-Messenger Astronomy (MMA) depends on robust software ecosystems and fast alerts.

Critical infrastructure components include alert brokers (e.g., Fink; Möller et al. 2020, ALERCE; Förster et al. 2021, and ANTARES; Matheson et al. 2021), among others, for data processing and distribution, as well as Target Observation Managers (TOMs) such as SkyPortal (van der Walt et al. 2019; Coughlin et al. 2023) that coordinate follow-up resources. Early classification is paramount for optimizing spectroscopic follow-up of rare transients such as Tidal Disruption Events (TDEs), kilonovae, and Fast Blue Optical Transients (FBOTs). An example of this is the use of available spectra to prevent misclassification, as demonstrated by González-Bañuelos et al. (2025), which identified 34 misclassified supernovae and revised the estimated core-collapse supernova rate.

In MMA contexts, rapid classification significantly reduces candidate pools for gravitational-wave follow-up (Stachie et al. 2020). Although fast transients can be discovered without external triggers (e.g. ZTFReST; Andreoni et al. 2021), current limitations are evident. ZTF’s Survey I (2018–2020) secured spectroscopy for 30 TDEs (Hammerstein et al. 2023), whereas FBOTs are often found in archival searches where follow-up is impractical (Ho et al. 2023).

ZTF already generates $\sim 10^5 - 10^6$ alerts each night (Patterson et al. 2019), and LSST (Ivezić et al. 2019) is poised to scale this to $\sim 2 \times 10^7$. Therefore, robust machine learning (ML) frameworks are essential for timely classification, anomaly detection, and deeper archival data exploration.

Existing classification models have historically specialized along source-type boundaries. Some focus on periodic or quasi-periodic variable stars (for example, see

Jamal & Bloom 2020; Rizhko & Bloom 2025; Chaintan et al. 2024; Zuo et al. 2025), while others target explosive transients such as supernovae (for example, see Villar et al. 2019; Hosseinzadeh et al. 2020; Fremling et al. 2021; Pimentel et al. 2022; Zhang et al. 2024; Sharma et al. 2025). Very few frameworks aim to classify both regimes simultaneously; a major limitation for real-time pipelines processing heterogeneous alert streams.

Some efforts, such as the Real-time Automated Photometric IDentification (RAPID; Muthukrishna et al. 2019) and follow-up work (Gupta et al. 2024), have attempted mixed-source classification, but rely exclusively on simulated ZTF light curves. LSST-driven initiatives like the Photometric LSST Astronomical Time-series Classification Challenge (PLAsTiCC; The PLAsTiCC team et al. 2018; Kessler et al. 2019; Malz et al. 2019; Hložek et al. 2023) and its successor ELAsTiCC pushed the field forward, fostering the development of transformer-based classifiers (Allam & McEwen 2023; Cabrera-Vives et al. 2024) and highlighting the importance of anomaly detection for rare source discovery (Villar et al. 2021). However, these benchmark datasets were also based entirely on simulation.

Practical classifiers integrated into broker pipelines (e.g., Fink; Möller et al. 2020, ALERCE; Sánchez-Sáez et al. 2021, and ANTARES; Narayan et al. 2018; Matheson et al. 2021) have been optimized for real-time use, but are typically restricted to single-modality inputs, most often photometric light curves. There are already some multi-modal classifiers in production, for example Neira O. et al. (2024); Rehemtulla et al. (2025); Duev & van der Walt (2021); Carrasco-Davis et al. (2021). However, the classification focus differs from that in this paper. For example, in Neira O. et al. (2024) the primary interest is in distinguishing moving objects and filtering spurious detections rather than a comprehensive astrophysical typing.

In the multimodal domain, models like AstroCLIP (for galaxy images and spectra; Parker et al. 2024), PAPERCLIP (for image–text matching; Mishra-Sharma et al. 2024), and LAVA (for unifying multimodal astronomical data streams; Zaman et al. 2025) represent a shift toward more generalized frameworks. Stellar classification models (Leung & Bovy 2023) have similarly adopted CLIP-style contrastive training (Radford et al. 2021).

More recent advances in foundation models offer new opportunities for generalization and transfer. Time-domain models like AstroM³ (Rizhko & Bloom 2025) and MAVEN (Zhang et al. 2024) demonstrate strong performance within specific source domains, but none currently support a unified treatment of both transients and

variable stars using real observational data (i.e. that these do not demonstrate cross-survey functionality). Moreover, they do not incorporate all four key input modalities (photometry, images, metadata, and spectra) which are critical for early-time decision making. This fragmentation limits the utility of current systems in real-time alert pipelines and impedes retrospective discovery, as highlighted by recent archival studies uncovering missed transients in ZTF (Aleo et al. 2022).

To address these gaps, we present **AppleCiDER** (Applying multimodal learning to Classify transient Detections Early), a unified multimodal ML framework for time-domain classification. It is built to serve two synergistic purposes: (1) a production-ready classifier that fuses photometry, image cutouts, and metadata for early classification of both transients and variable sources in ZTF and LSST pipelines; and (2) a foundation model architecture incorporating spectra to enable archival reanalysis and cross-domain generalization.

Section 2 describes the data and preprocessing. Each modalities model is presented separately: photometry (Sec. 3), images/metadata (which we treat as a single modality due to their presence in the alert packets; Sec. 4), and spectra (Sec. 5). Sec. 7 summarizes the results and discusses the future plans for **AppleCiDER**.

The **AppleCiDER** pipeline is publicly available at <https://github.com/skyportal/applecider>. We release the software and training set we used from the Bright Transient Survey and full ZTF ID listing for reproducibility.

2. DATASET

Alert and photometry data from ZTF are stored in **Kowalski**¹, an open-source, multi-survey data archive and alert broker (Duev et al. 2019), from which we query these modalities. For sources with spectra, we gather them from **Fritz**², the version of **SkyPortal** (van der Walt et al. 2019; Coughlin et al. 2023) used in production by the ZTF collaboration. Further spectra were gathered from public data repositories including **WISeREP** (Yaron & Gal-Yam 2012), **SDSS** (Abdurro'uf et al. 2022), **DESI** (DESI Collaboration et al. 2024), as well as the **GROWTH Marshal** (Kasliwal et al. 2019) and **Transient Name Server**³.

All ZTF sources in the dataset⁴ were classified into one of the transient categories (Table 1) with probabil-

ity ≥ 0.6 using non-machine learning methods. Sources were selected regardless of magnitude, though half originate from the Bright Transient Survey (Fremling et al. 2020; Perley et al. 2020; Rehemtulla et al. 2024). In the following, we describe the pre-processing steps for each modality.

Table 1. Unified Class Distribution by Object Type and Dataset. Note that 9376 out of 18245 objects are from BTS.

Type	Number of objects
SN Ia	6322
SN Ib	145
SN Ic	153
SN II ^a	695
SN IIb	126
SN IIP	627
SN IIn	234
CV ^c	963
AGN ^d	8905
TDE	75
Total	18245

*SN I: Type I Supernovae, ^aType II Supernovae, ^b Cataclysmic Variables, ^c Active Galactic Nuclei

2.1. Alerts

Alerts are triggered by a $\geq 5\sigma$ change in brightness relative to historical reference images. These events arise from genuine astrophysical sources (e.g., transients, variable stars, or moving objects like asteroids) or artifacts (Graham et al. 2019). Each alert packet contains contextual information, including metadata features and a triplet of 63×63 pixel image cutouts centered on the transient candidate: (i) a *science image* (new observation), (ii) a *reference image* (co-add of historical data), and (iii) a *difference image* (subtraction result). Multiple alerts may be generated per object over the survey lifetime, reflecting distinct activity epochs (Masci et al. 2019). Alert data include photometry in the ZTF-*g*, ZTF-*r*, and ZTF-*i* filters (Dekany et al. 2020), which are converted from magnitudes to fluxes.

While alerts do not include spectroscopic information, we incorporate such data when available for specific objects (for details, see Sec. 2.2). A unified class Distribution by object type and dataset is given in Table 1.

Our analysis includes 17 features, which we include based on experience from **BTSBot** (Rehemtulla et al. 2024), as listed in Table 2. For a complete description of the alert metadata, we refer the reader to the *ZTF*

¹ <https://github.com/skyportal/Kowalski>

² <https://github.com/fritz-marshal/fritz>

³ <https://www.wis-tns.org/>

⁴ Complete source list: <https://github.com/skyportal/applecider>

*Alert Schema*⁵. Additional details on the photometric data are provided in Sec. 3.

Table 2. Overview of metadata features adopted from BTSBot.

Feature name	Description [unit]
Alert Metadata	
sgscore{1,2}	Star/galaxy classification score for two closest PS1 objects
distpsnr{1,2}	Angular separation to two closest PS1 sources [arcsec]
ra	Right Ascension [deg]
dec	Declination [deg]
magpsf	Magnitude from PSF-fit photometry [mag]
sigmapsf	1 σ uncertainty in magpsf [mag]
chinr	χ parameter of nearest source in reference image PSF-catalog
sharpnr	Shape measurement of nearest reference object
sky	Background sky brightness [data units]
classtar	Star/Galaxy classification score from SExtractor
ndethist	Spatially-coincident detections within 1.5 arcsec
ncovhist	Times candidate position on any field/readout-channel
scorr	Peak pixel signal-to-noise ratio in detection
nmtchps	Source matches from PS1 catalog within 30 arcsec
diffmaglim	Magnitude for 5 σ detection [mag]
Custom Metadata	
age	Total duration: days_since_peak + days_to_peak
nndet ^a	Difference: ncovhist - ndethist (Non-detections)

Notes. PSF = Point Spread Function. S/N = Signal-to-noise ratio.
^aDerived following Carrasco-Davis et al. (2021)

2.2. Spectra

Although alert packets themselves do not contain spectroscopic data, we associate each alert with a single archival spectrum when available. These spectra are primarily obtained with the Spectral Energy Distribution Machine (SEDM; Blagorodnova et al. 2018; Rigault et al. 2019; Kim et al. 2022) with additional observations contributed by various other instruments (for example, see Table 3). For consistency, we attach the spectrum that is temporally closest to the object’s first photometric observation for the multimodal model, while the spectral-only model is trained using all available spectra per object to capture spectral evolution. Spectral labels are drawn from transient classifications provided by the Transient Name Server (TNS) or derived from internal classification pipelines.

Each spectrum undergoes a standardized preprocessing pipeline designed to restore intrinsic spectral features and produce input suitable for deep learning models. The first step involves correcting for redshift. Given a spectroscopic redshift z , we transform the observed wavelength axis to the rest-frame using

$$\lambda_{\text{rest}} = \frac{\lambda_{\text{obs}}}{1+z}. \quad (1)$$

We then restrict all spectra to the rest-frame wavelength range of 3850 Å to 8500 Å. Spectra are linearly interpolated to a fixed grid of 4096 evenly spaced points within this range. Spectra that do not fully cover the target wavelength range yield undefined values at certain grid points during interpolation; we set these regions to zero to indicate the absence of valid data. The resulting flux arrays are then standardized using Z-score normalization:

$$f_{\text{norm}} = \frac{f - \mu}{\sigma}, \quad (2)$$

where μ and σ are the mean and standard deviation computed from the valid (nonzero) flux values of each spectrum.

This procedure ensures that all spectra are aligned in rest-frame wavelength, resampled to a fixed resolution, and normalized in scale, providing consistent and model-friendly inputs.

3. PHOTOMETRY

Early work in photometric time-series classification focused on extracting handcrafted features (Nun et al. 2015; Richards et al. 2011) from multi-band light curves—such as parametric fits (Karpenka et al. 2012; Lochner et al. 2016; Noebauer et al. 2017; Villar et al. 2019), principal component analyses (Ishida & de Souza 2013; Lochner et al. 2016), and wavelet or Gaussian process models (Varughese et al. 2015; Boone 2019). Class imbalance and limited coverage of rare transients made simulated datasets like the SNPhotCC (Kessler et al. 2010) and PLAsTiCC key benchmarks.

As data volumes have grown, deep learning has become increasingly dominant for machine-learning based classifications. Specifically, Transformer models have shown state-of-the-art performance on both synthetic and real photometric datasets, with architectures such as TimeModAttn (Pimentel et al. 2022) and multimodal models like ATAT (Cabrera-Vives et al. 2024) and AstroM³ leveraging attention to integrate photometry with metadata and spectra.

Motivated by these advances, we adopt two attention-based encoders tailored to ZTF light curves of explosive transients. The first is the Informer (Zhou et al. 2020), which employs sparse attention to efficiently model long

⁵ <https://zwickytransientfacility.github.io/ztf-avro-alert/schema.html>

Table 3. Spectroscopic observations by instrument.

Spectrograph (or Survey)	Number of Spectra
SEDM ¹	5952
SDSS ²	2980
SPRAT ³	308
DBSP ⁴	303
EFOSC2 ⁵	196
DESI ⁶	158
LRIS ⁷	145
SNIFS ⁸	125
DeVeny	79
FLOYDS-N, FLOYDS-S	63
ALFOSC ⁹	62
DIS ¹⁰	56
Goodman	24
AFOSC ¹¹	17
Gemini-N, Gemini-S	12
Other Spectrographs ¹²	76

¹Spectral Energy Distribution Machine (SEDM) ²Sloan Digital Sky Survey (SDSS) ³Spectrograph for the Rapid Acquisition of Transients (SPRAT) ⁴Double Spectrograph (DBSP) ⁵ESO Faint Object Spectrograph and Camera (EFOSC2) ⁶Dark Energy Spectroscopic Instrument (DESI) ⁷Low-Resolution Imaging Spectrograph (LRIS) ⁸SuperNova Integral Field Spectrograph (SNIFS) ⁹Alhambra Faint Object Spectrograph and Camera (ALFOSC) ¹⁰Dual Imaging Spectrograph (DIS) ¹¹Asiago Faint Objects Spectrograph and Camera (AFOSC) ¹²Spectra from spectrographs with less than 10 counts

sequences and has proven effective in **AstroM**³. The second, a dense Transformer with a learnable classification token ([CLS]-Transformer; Devlin et al. 2018; Zerveas et al. 2020), is designed for early-epoch classification under limited observations. This architecture is enhanced with learnable temporal embeddings and trained in two stages: self-supervised pretraining and supervised finetuning. Below, we present key information about the input data, model architecture, and training. For detailed discussion on these aspects, data preprocessing and ablation study comparison with other models, readers are referred to Fontinele Nunes, et al. (2025, in prep.).

3.1. Input Representation

Raw photometric observations $(t_i, f_i, \sigma_{f,i}, b_i)$ are first grouped into events. Measurements within a 12 hr

Table 4. Input Features for Attention-Based Classification

Feature	Description
Δt_n	Time since first detection ($t_n - t_1$)
δt_n	Time since previous observation ($t_n - t_{n-1}$)
$\log_{10}(f_n)$	Log-scaled flux with floor thresholding
$\sigma_{\log f, n}$	Uncertainty on log-flux (propagated from $\sigma_{f, n}$)
\mathbf{b}	One-hot encoding vector for g , r , or i band

window are temporally merged using inverse-variance weighting, resulting in a set of effective observations.

Each merged observation is encoded as a 7-dimensional feature vector designed to capture both photometric properties and temporal context (Table 4). The temporal features ($\Delta t_n, \delta t_n$) explicitly encode absolute and relative timing information, addressing the irregular sampling inherent in survey data. Log-scaled flux with uncertainty propagation ensures numerical stability while preserving physical interpretability. Filter encoding and color availability flags enable the model to handle multi-band observations and adapt to varying photometric coverage.

3.2. Model Architecture

Our [CLS]-Transformer architecture addresses three key requirements for transient classification: handling irregular temporal sampling, integrating multi-band photometry, and enabling early classification from partial light curves.

Temporal Embedding.—Rather than fixed positional encodings, we employ learnable temporal embeddings that explicitly model the continuous nature of astronomical time series. The temporal encoding for observation n combines linear and sinusoidal components. This formulation captures both monotonic evolution (linear trend) and potential periodic behavior (sinusoidal terms) while adapting to the specific temporal scales present in the training data.

Feature Projection and Sequence Construction.—Each preprocessed observation vector \tilde{x}_n is projected into the model’s embedding dimension through a learned transformation. The final input representation combines photometric features with temporal context. A special classification token [CLS] is prepended to each sequence, providing a dedicated representation for downstream classification that can aggregate information across all observations.

Transformer Encoder.—The encoder consists of L standard Transformer layers with multi-head self-attention and feedforward sublayers. The self-attention mechanism enables each observation to attend to all others in the sequence, naturally handling irregular sampling and discovering relevant temporal relationships for classification. The final [CLS] representation is normalized and passed through a classification head.

3.3. Training Procedure

The performance of the model is evaluated using a horizon sweep approach with multiple metrics: macro-average precision recall (Macro-AUPRC), balanced precision, and Top-k inclusion rates. These metrics quantify classification performance across different observational depths and class distributions.

A two-stage training procedure is employed, designed to leverage both unlabeled photometric data for light curve reconstruction and labeled data for transient classification.

Self-Supervised Pretraining.—To initialize the encoder with light-curve-specific structure, the model is first trained using masked event modeling on light curves spanning 100 days since the first trigger. Roughly 30% of observations are masked, and the model is trained to reconstruct key photometric features using a combination of three losses – a mean squared error loss on the flux values, a cross-entropy loss on the photometric band labels, and a mean squared error loss on the relative timing between observations. Each of these components is weighted by a corresponding hyperparameter to balance their contributions.

Supervised Fine-tuning.—For classification, the pre-trained model is fine-tuned using truncated light curves (e.g., up to 100 days). We use weighted focal loss (Lin et al. 2018) and augmentation of the TDE class to handle the imbalance inherent to the dataset. Two fine-tuning strategies are considered: (i) full-model training from the start; and (ii) training only the classification head initially, followed by gradual unfreezing of the encoder layers with lower learning rates.

3.4. Results

We evaluate the classification performance of our adopted model in comparison to the **Informer** encoder used in **AstroM³**, both fine-tuned on light curves cut-off at 30 days since the first observation. As shown in Table 5, our model achieves a significantly higher overall accuracy of 88% compared to 59% from the **Informer** baseline.

Our model shows consistent improvements across all transient classes, and better per-class AUC scores. It ex-

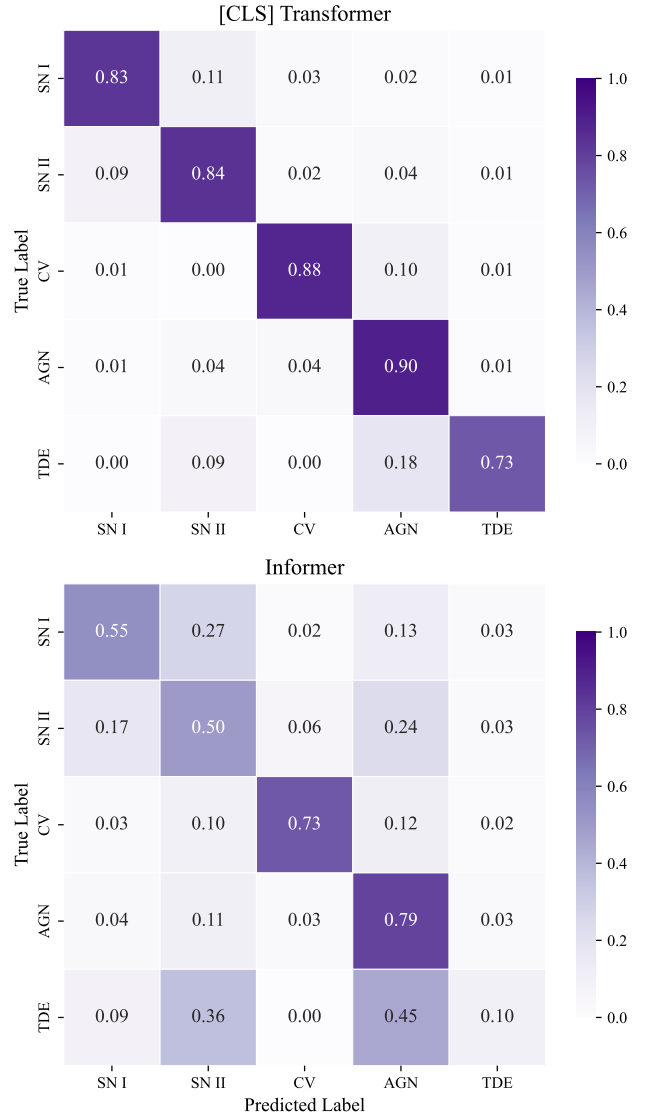


Figure 1. Confusion matrix comparison between our proposed Transformer encoder (*top*) and the Informer encoder from **AstroM³** (*bottom*).

cells with challenging classes like TDEs, achieving 0.95 AUC versus 0.82. The confusion matrix in Fig. 1 highlights our model’s enhanced class separability and reduced ambiguity.

4. IMAGES: AstroMiNN

Traditional astronomical transient classification relied on feature-based machine learning models (Bloom et al. 2012; Brink et al. 2013), including photometric redshift estimation (Carrasco Kind & Brunner 2013) and supernova classification (Villar et al. 2020). The advent of CNNs revolutionized image processing, enabling morphology classification (Dieleman et al. 2015), strong lens detection (Lanusse et al. 2018), and real-bogus filtering

Table 5. Classification Performance Comparison for Photometry only.

Model	Informer	[CLS] Transformer
Overall Accuracy (%)	59 ± 0.3	88 ± 0.4
AUC Values by Class		
Macro-average	0.89	0.97
SN I	0.94	0.99
SN II	0.87	0.96
CV	0.90	0.97
AGN	0.95	0.99
TDE	0.82	0.95

(Duev et al. 2019). Recent multi-input architectures (Carrasco-Davis et al. 2021; Duev & van der Walt 2021) combine imaging and tabular data, directly inspiring BTSbot’s (Rehemtulla et al. 2024) design.

BTSbot utilizes a multi-input CNN combining images and metadata features (i.e., see Tab. 2) to identify bright extragalactic transients and infant supernovae (Rehemtulla et al. 2025) in ZTF. This approach processes images and features separately and then combines them to improve classification accuracy over single-input methods. The extracted features are processed by a multi-layer perceptron (MLP; Rumelhart et al. 1986), while image data is handled by a convolutional branch.

The existing methods of analyzing images and metadata only use two MLPs, one for the metadata, and another to fuse the image and metadata features. While this achieves relatively good results for large datasets and roughly even class distributions, the performance decreases in cases of uneven class distribution and limited datasets. To tackle this challenge, we introduce **AstroMiNN**, a specialized multimodal neural network that integrates convolutional vision backbones with structured expert towers for metadata data.

The **AstroMiNN** architecture is explicitly designed to incorporate domain-specific structure, leveraging both the spatial and physical properties of transient detections. The overall architecture is illustrated in Figure 2 and for each part of the architecture, we give more details in the following.

4.1. Metadata Processing Towers

The metadata stream is decomposed into thematic groups and processed by independent *Residual Tower Blocks* (He et al. 2016). Each tower captures distinct scientific parameters:

- **PSF Tower:** Shape parameters and PSF sharpness (e.g., `chir`, `sharpnr`, and `classtar`).

- **Magnitude Tower:** Photometric statistics such as PSF magnitude and peak magnitude so far (e.g., `magspsf`, `sigmagspsf`, and `diffmaglim`).
- **Light Curve Tower:** Historical variability and timing-based metrics (e.g., `age`, `ndethist`, `ncovhist`, and `nmondet`).
- **Spatial Tower:** Spatial observables including sharpness and source confusion (e.g., `sky`, `nmtchps`, `scorr`).
- **Nearest Source Towers:** Proximity and likelihood features from the nearest detected source (`sgscore` and `distpsnr` pairs).
- **Coordinate Tower:** Right Ascension (`ra`) and Declination (`dec`), optionally modulated with sinusoidal encodings.
- **Mega Tower:** A comprehensive tower trained on all metadata features jointly.

Each tower is composed of a small feedforward block with **GELU activations** (Hendrycks & Gimpel 2016) and residual connections (He et al. 2016). Optional **gating heads** allow for dynamic feature masking based on learned confidence scores (Shazeer et al. 2017).

We construct towers in this way such that each metadata feature is considered primarily in relation to a select few other related metadata items. This approach requires that each metadata feature is first expanded with its most directly associated features before forming more distant connections. For example, magnitude measurements should be expanded with their associated error values before establishing further feature linkages, thus enforcing any necessary conditionality among related features. Given that these are merely initial expansions, each tower is designed to be lightweight, incorporating only two linear expansion layers and a skip path, all maintaining the same-dimensional output.

4.2. Image Feature Encoder

For the imaging stream, we adopt a **ConvNeXt-Tiny** backbone (Liu et al. 2022) pre-trained on ImageNet (Deng et al. 2009; Narihira et al. 2021). Our encoder, termed “Split Head ConvNeXt”, incorporates two specialized custom heads to process the images. The main head projects features into a classification embedding space, providing the primary pathway for feature extraction and representation learning. Complementing this, the **auxiliary head** performs dynamic channel modulation using a per-sample sine-based positional embedding that incorporates RA/Dec coordinates, allowing

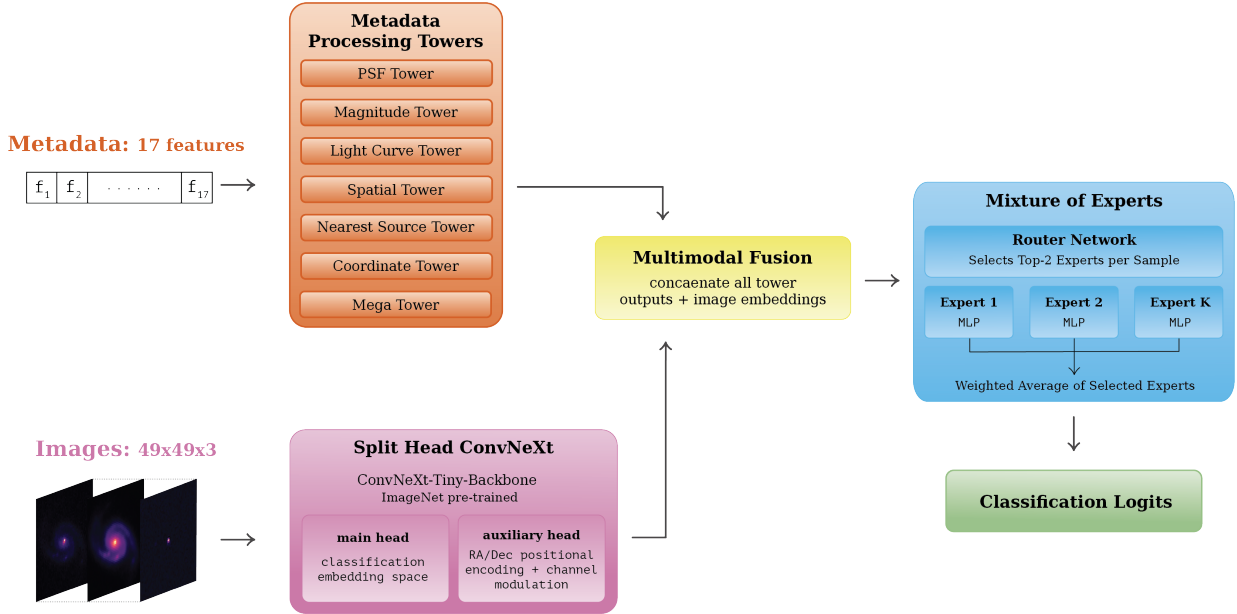


Figure 2. AstroMiNN Architecture. Metadata features are routed through specialized residual towers before being fused with image embeddings from a dual-head ConvNeXt-based encoder. The combined representation is processed by a Mixture-of-Experts (MoE) module, with expert selection governed by a router network.

the model to spatially contextualize each observation within the celestial coordinate system.

The input images consist of triplets of 49×49 pixel cutouts (see Sec. 2; Rehemtulla et al. 2024; Carrasco-Davis et al. 2021). Beyond these standard channels, the model processes additional information that encodes the radial distance from the cutout center and the embedded sky coordinates, enriching the spatial and positional context available to the network during feature extraction and classification.

4.3. Fusion and Expert Routing

While tower gating mechanisms (e.g., softmax- or sigmoid-weighted sums) have been explored before in astro-ML work (Vanderplas et al. 2012; Ivezić et al. 2014), they often rely on the strong assumption that individual tower features are linearly combinable into a global representation. Instead, we adopt a different approach; tower outputs are concatenated (Kiela et al. 2020) and passed to a shared fusion space without weighting. This strategy enables the network to learn richer feature interactions through multiple fusion experts – each implemented as an independent MLP – that operate over the full multimodal embedding.

Subsequently, the unified representation is processed by a Mixture of Experts (MoE) module (Shazeer et al. 2017; Fedus et al. 2022; Mu & Lin 2025). This consists of (i) a router network that computes a probability distribution over K expert heads and selects the top-2 experts per sample, and (ii) a set of K expert MLPs,

each acting as a lightweight classifier. Expert load balancing follows Lepikhin et al. (2020).

This avoids forcing towers into a globally interpretable weighting scheme and instead allows each expert to adaptively specialize on complex feature interactions. The final output logits are computed as a soft aggregation of the top- k expert predictions, promoting competition among experts while maintaining interpretability through expert load monitoring.

4.4. Loss Function and Expert Specialization

In addition to traditional classification losses such as Focal (Lin et al. 2018), we apply a regularization term that encourages *expert specialization* (Eigen et al. 2014; Mu & Lin 2025). The router is trained to align expert weights with class-specific priors using a target expert assignment (e.g., class label modulo number of experts). This is enforced via an auxiliary MSE loss on expert weights:

$$\mathcal{L}_{\text{total}} = \mathcal{L}_{\text{focal}} + \lambda \cdot \text{MSE}(w_{\text{expert}}, w_{\text{ideal}}) \quad (3)$$

where λ controls the contribution of the specialization term.

4.5. Results

After evaluating various models, we found that the BTSbot model provided the best classification results among the existing architectures we tried. Consequently, we compare our new model AstroMiNN with BTSbot. Table 6 displays the AUC scores for both mod-

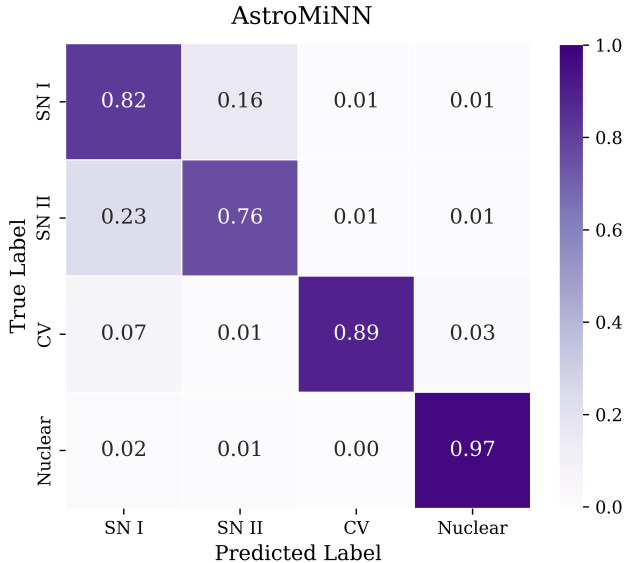


Figure 3. Confusion matrix for *AstroMiNN* model.

els across four classes, indicating that *AstroMiNN* performs better classification for nuclear and CV events. The confusion matrix is given in Fig. 3.

Table 6. Comparison of AUC scores between *AstroMiNN* and *BTSbot* models.

Class	<i>AstroMiNN</i>	<i>BTSbot</i>
SN I	0.83	0.83
SN II	0.76	0.78
CV	0.99	0.97
Nuclear	0.99	0.97

5. SPECTRA: SpectraNet

Spectroscopic classification using machine learning often operates on flux-wavelength sequences that have been interpolated onto a fixed grid, allowing uniform input dimensions across a dataset. Recent advances in deep learning have shown promising results in this domain. For instance, *GalSpecNet* (Wu et al. 2024) applies convolutional neural networks (CNN) to 1D spectra for transient classification. The same model has also been adopted in the *AstroM³* pipeline. Another example, *SNIascore* (Fremling et al. 2021), leverages recurrent units such as BiLSTM and GRU layers for real-time classification of low-resolution Type Ia supernova spectra. Similarly, *CCSNCore* (Sharma et al. 2025) adopts a multi-input architecture designed specifically to extract and classify spectroscopic features of core-collapse supernovae. Another approach has been presented in

Strano Moraes et al. (2025), where vision transformers for spectra data are used.

Although existing methods have achieved notable progress in spectral classification, several critical limitations remain. In particular, supernova classification strongly depends on localized spectral features – such as the shape, depth, and width of absorption lines – which often vary significantly across subtypes. Recurrent models, such as BiLSTM and GRU, are well-suited for modeling long-range dependencies. However, they may overlook important local structures critical to supernova subclass discrimination. Moreover, to reduce computational cost, RNN-based models often restrict input sequence length, which can lead to information loss and reduced classification accuracy. While convolutional architectures are naturally better at capturing local patterns, most existing 1D CNN-based models are relatively shallow and lack the expressive capacity to extract complex or multi-scale spectral features. This becomes particularly limiting when dealing with noisy observations or spectra that evolve over time.

To address these issues, the final adopted model is a deep, multi-scale 1D convolutional architecture—*SpectraNet* (Xu, et al. 2025, in prep.). This model is designed to improve the extraction of localized spectral signatures while maintaining computational efficiency and achieving higher classification performance. As shown in Xu, et al. 2025, in prep., this architecture outperforms traditional 1D CNN and Transformer baselines in supernova spectral classification.

5.1. Training Details

The *SpectraNet*-1D (Xu, et al. 2025, in prep.) network consists of two main components, a convolutional feature extraction backbone followed by fully connected classification layers.

Convolutional Backbone—The network begins with five sequential *SpectraBlocks* that progressively reduce the spectral resolution while increasing the feature depth. The input spectrum (size 1×4096) is processed through *SpectraBlocks* with sizes 32×1024 , 64×256 , 128×64 , 256×16 , and 1536×16 , respectively. Each *SpectraBlock* incorporates a multi-scale convolutional architecture that processes the input at three different scales (large, medium, and small) through parallel convolutional paths. The multi-scale features are concatenated and passed through layer normalization and batch normalization before being fed into a “TriPool1D” module. The “TriPool1D” component combines three pooling strategies (MaxPool, AvgPool, and MinPool) to capture diverse statistical representations of the spectral features. This is followed by a channel gate attention

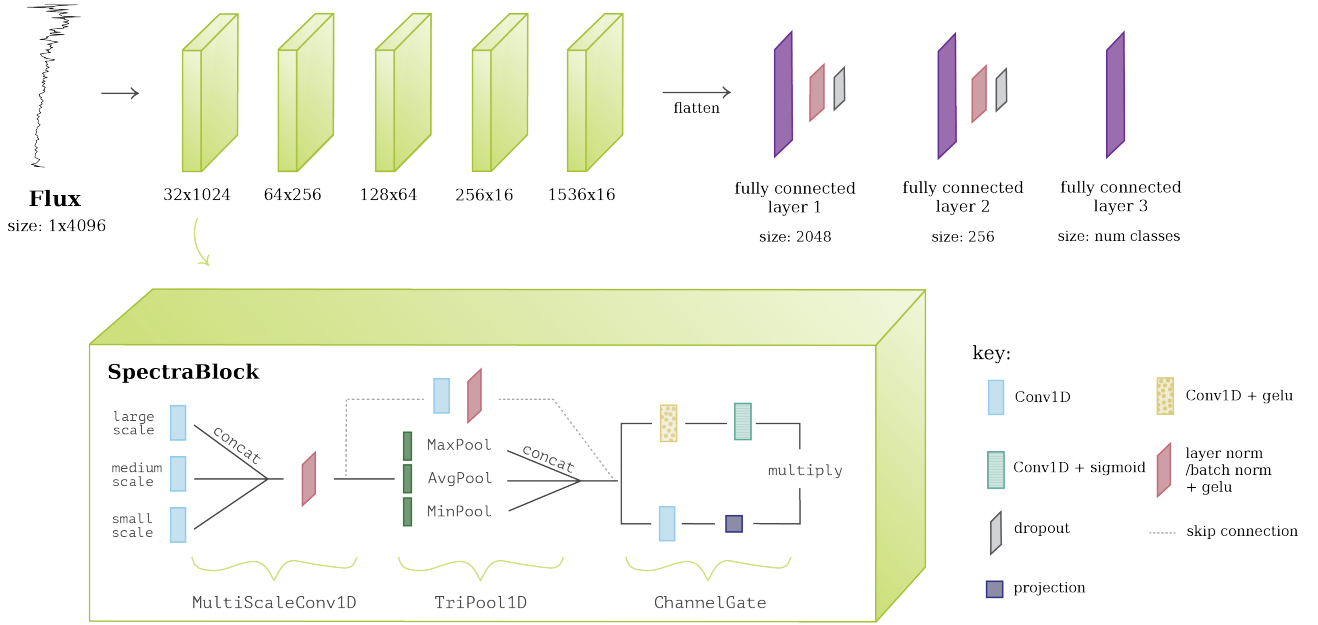


Figure 4. SpectraNet Architecture.

mechanism that applies sigmoid activation to selectively weight the feature channels, with a projection layer and skip connection to preserve important spectral information.

Classification Head—After the convolutional feature extraction, the output is flattened and processed through three fully connected layers. The first layer maps the 1536×16 feature tensor to 2048 dimensions, followed by a second layer reducing to 256 dimensions, and finally a classification layer outputting the number of target classes. Each fully connected layer incorporates layer normalization, batch normalization, and GELU activation functions to ensure stable training and effective feature representation.

The model is trained using the AdamW optimizer (Loshchilov & Hutter 2019), with the learning rate selected via Optuna (Akiba et al. 2019). A linear warm-up schedule is followed by a cosine annealing learning rate schedule (Loshchilov & Hutter 2017), and early stopping is triggered based on a composite validation score with a fixed `patience` threshold.

To address class imbalance, we use Focal Loss (Lin et al. 2018) with class-balanced weighting (Cui et al. 2019). An Exponential Moving Average (EMA; Tarvainen & Valpola 2018) of the model weights is maintained and used for evaluation and model saving. We also adopt automatic mixed-precision (AMP) training to reduce memory usage and accelerate convergence. Model selection is based on the highest composite score on the validation set, combining accuracy, macro F1, and Top-3 accuracy.

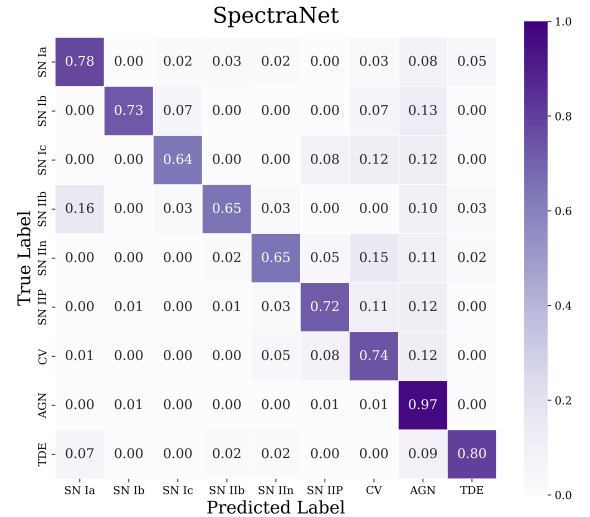


Figure 5. Confusion Matrix for SpectraNet model.

This architecture is specifically designed for 1D spectral data, leveraging multi-scale feature extraction and attention mechanisms to capture both local spectral features and global patterns essential for accurate astronomical object classification. A diagram of the architecture is given in Fig. 4.

5.2. Results

Table 7 presents a detailed comparison of classification performance between GalSpecNet (Wu et al. 2024) and our proposed SpectraNet across nine astronomical object classes. SpectraNet demonstrates superior overall accuracy of 87%, outperforming GalSpecNet’s 83%. In

terms of class-wise AUC scores, **SpectraNet** consistently achieves higher performance across all categories. Notable improvements are observed for challenging classes such as SN Ic (AUC improved from 0.95 to 0.97), SN IIP (0.96 to 0.99), and TDE (0.96 to 0.99). Importantly, **SpectraNet** does not underperform in any category; all class-specific AUC scores are above 0.96. Figure 5 further illustrates the model’s confusion matrix using the **SpectraNet**-2D variant, highlighting substantial improvements in distinguishing core-collapse supernovae (e.g., SN IIP, I Ib, I In) and non-SN transients such as AGN, CV, and TDE.

Table 7. Classification Performance Comparison

Model	SpectraNet	GalSpecNet
Overall Accuracy (%)	87.0 ± 0.5	82.6 ± 0.6
AUC Values by Class		
Micro-average	0.98	0.96
SN Ia	0.99	0.97
SN Ib	0.97	0.94
SN Ic	0.97	0.95
SN IIP	0.99	0.96
SN I Ib	0.96	0.95
SN I In	0.98	0.98
AGN	0.97	0.96
CV	0.99	0.97
TDE	0.99	0.96

6. AppleCiDER PERFORMANCE

Table 8. Common dataset derived from objects in Tab. 1

Type	Objects	Alerts
SN I	4830	22791
SN II	1014	4520
CV	279	1262
AGN	1251	2375
TDE	36	117
Total	7410	31065

AppleCiDER leverages the neural network architectures presented in the previous Sections 3-5, and performs class-wise averaging over their predicted probabilities. All networks are trained jointly on the same dataset – rather than on disjoint subsets as in earlier experiments – and are evaluated collectively on a shared

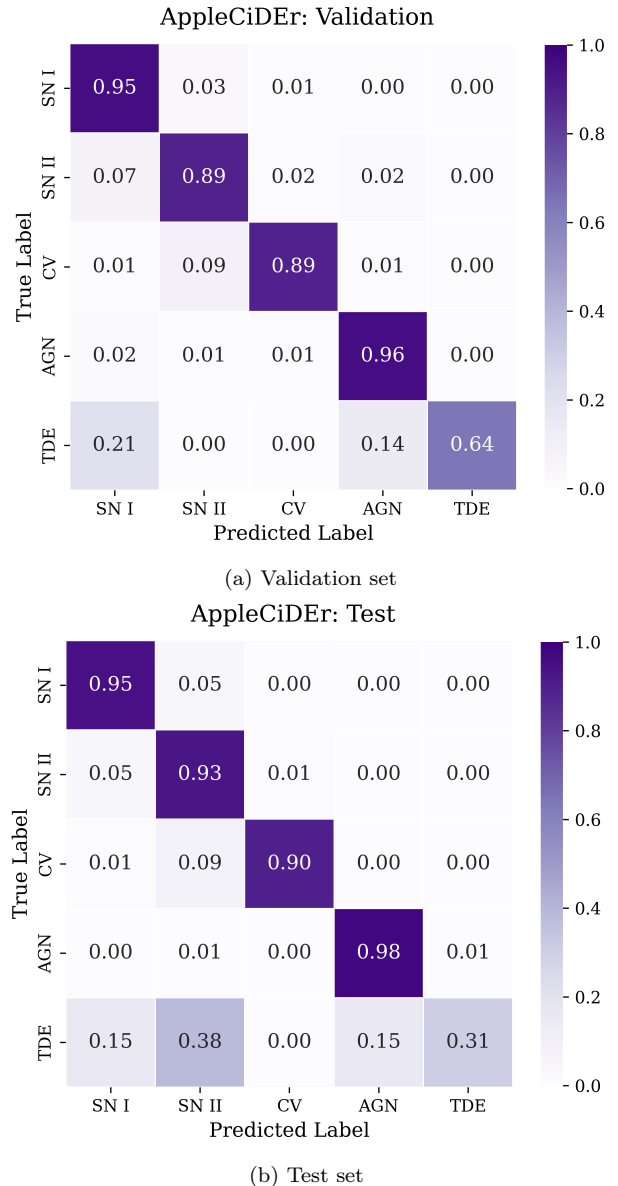


Figure 6. AppleCiDER performance. Normalized confusion matrices for the (a) validation and (b) test sets. The classifier shows strong performance across SN I, SN II, CV, and AGN classes. TDE classification is notably more challenging, with substantial confusion with SN I, SN II, and AGN.

test set. The dataset is chosen based on common⁶ data for ten days (see Tab. 1). As shown in Fig. 6, it demonstrates robust classification performance for most transient classes. On the validation set (Fig. 6a), SN I, SN II, CV, and AGN are correctly classified with accuracies ranging from 89% to 96%. However, the TDE class presents challenges, with only 64% correct identi-

⁶ Available data for photometry, spectra, images and metadata.

fication and confusion primarily with SN I (21%) and AGN (14%).

On the test set (Fig. 6b), similar trends are observed. SN I, SN II, CV, and AGN remain well separated, with classification accuracies of 95%, 93%, 90%, and 98%, respectively. The TDE class exhibits a more pronounced misclassification, particularly toward SN II (38%) and SN I/AGN (15% each), achieving only 31% accuracy.

This suggests that while **AppleCiDER** generalizes well for common transients, TDE detection remains an area for targeted improvement. The reason for this is due to limited samples from this particular case.

7. DISCUSSION

AppleCiDER introduces a unified, multimodal framework that marks a substantial advancement in time-domain astronomy. By combining photometry, image cutouts, metadata, and spectral data, the model bridges a long-standing gap in survey pipelines, which traditionally process these modalities individually or through specialized models. Prior efforts have typically focused on specific source classes – such as supernovae or variable stars – or have operated only on simulated datasets. In contrast, **AppleCiDER** is designed and validated using real ZTF alert data, delivering robust and generalizable performance across a diverse range of transients and variables. This capability addresses a critical limitation in existing pipelines, which rely on modular, single-modality classifiers to process complex and heterogeneous data streams.

There are several core architectural innovations underpinning this progress. Our [CLS]-Transformer, adopted from Fontinele Nunes, et al. 2025, in prep.), enables classification within the first few nights of observations, which is crucial for rapid response to targets such as TDEs. We also introduce a new network for image classification, the **AstroMiNN**, which leverages a metadata tower and the MoE fusion mechanism, achieving better performance compared to what exists currently. In the spectral domain, **SpectraNet-1D** (Xu, et al. 2025, in prep.) is adopted, which outperforms other pipelines, offering a powerful tool for low-resolution spectral classification.

These technical improvements translate directly into tangible astronomical benefits, including high classification AUCs for well-represented types such as SNIa and CVs, and up to 0.95 for more challenging classes like SNIc – enabling more efficient early-phase identification. This, in turn, helps prioritize limited follow-up resources, especially in the context of rare transients where spectroscopic confirmation is expensive or infeasible.

Importantly, the modularity of our approach also ensures that the framework is adaptable to upcoming large-scale surveys such as LSST, which will deliver tens of millions of nightly alerts. The auxiliary spatial head integrated into the **ConvNeXt** backbone – leveraging sky coordinates – adds contextual awareness to image classification, a capability absent in earlier systems.

However, some limitations remain. The model continues to face challenges associated with class imbalance, where rare types like TDEs and stripped-envelope supernovae (e.g., SN Ib/c) display increased classification uncertainty. Future versions of **AppleCiDER** will explore fusion techniques to combine networks for each modality rather than just averaging the output, while exploring different techniques to increase the performance for the TDEs.

In parallel, we are working on delivering this package for production. Our aim is to perform online classification with seamless integration into brokering pipelines. To this end, we are developing a real-time framework that leverages **AppleCiDER** to classify astronomical transients from ZTF in a low-latency, automated manner; we are currently deploying **AppleCiDER** into **SkyPortal** (van der Walt et al. 2019; Coughlin et al. 2023) as a classification pipeline and soon will be doing so within our broker **BOOM** (Burst & Outburst Observations Monitor) as a classification pipeline. As shown in Fig. 7, **AppleCiDER** will receive alerts from the broker system and perform source classification. Then, it will send this information to **SkyPortal** and suggest a follow-up spectroscopy using SEDM. The resulting spectra will be fed back into **AppleCiDER** for additional inference and refinement.

We also plan to extend this capability to LSST transients in the near future, specifically within **BABAMUL**, the public version of **BOOM** processing LSST alerts. However, generalization to LSST requires careful domain adaptation, particularly to accommodate differences in filter systems between ZTF and LSST, as highlighted by Muthukrishna et al. (2019).

These enhancements aim to solidify **AppleCiDER** not just as a classifier, but as a flexible and extensible engine for discovery in the time-domain sky. **AppleCiDER** ultimately provides a scalable and operational framework that bridges the divide between research-grade classifiers and real-time survey pipelines. Validated on more than 110,000 real alerts, it demonstrates the power of unified multimodal learning for immediate classification and retrospective discovery. With its public release, we invite the broader astronomical community to build on this work and shape the next generation of multimesenger science.

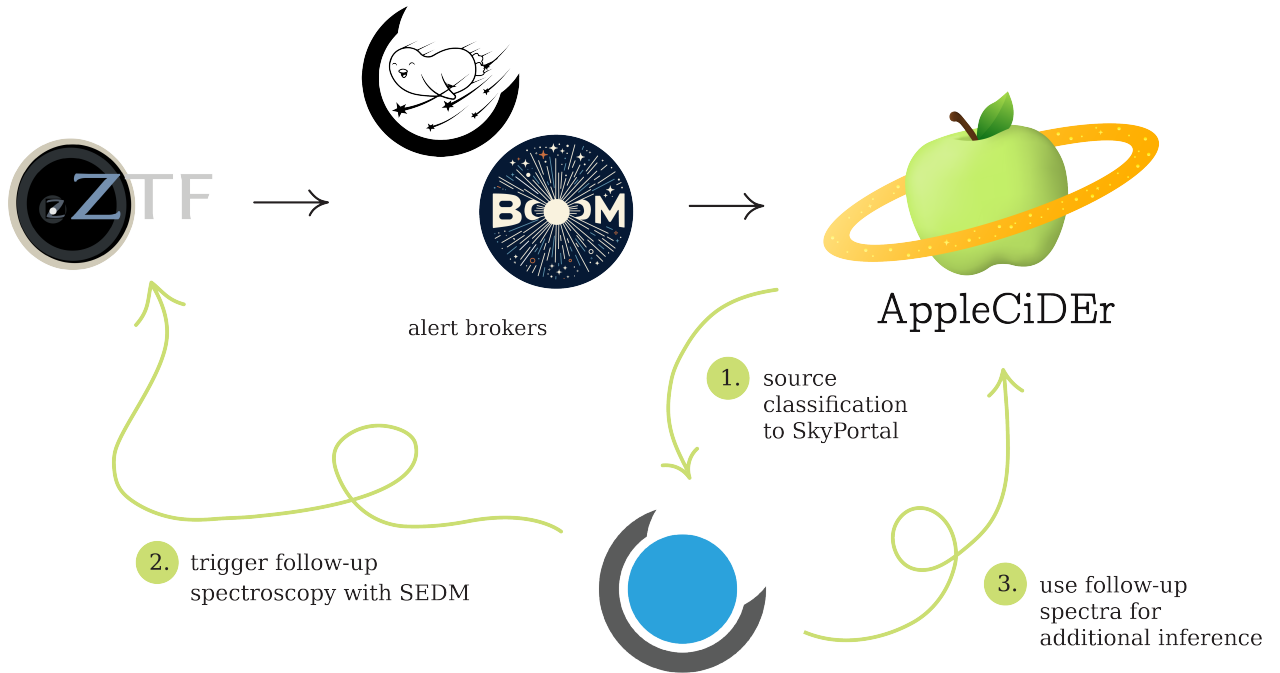


Figure 7. Planned ZTF production pipeline.

ACKNOWLEDGMENTS

The UMN authors acknowledge support from the National Science Foundation with grant numbers PHY-2117997, PHY-2308862 and PHY-2409481.

N.R. is supported by DoE award #DE-SC0025599. Zwicky Transient Facility access for N.R. was supported by Northwestern University and the Center for Interdisciplinary Exploration and Research in Astrophysics (CIERA).

Based on observations obtained with the Samuel Oschin Telescope 48-inch and the 60-inch Telescope at the Palomar Observatory as part of the Zwicky Transient Facility project. ZTF is supported by the National Science Foundation under Grants No. AST-1440341, AST-2034437, and currently Award #2407588. ZTF receives additional funding from the ZTF partnership. Current members include Caltech, USA; Caltech/IPAC, USA; University of Maryland, USA; University of California, Berkeley, USA; University of Wisconsin at Milwaukee, USA; Cornell University, USA; Drexel University, USA; University of North Carolina at Chapel Hill, USA; Institute of Science and Technology, Austria; National Central University, Taiwan, and OKC, University of Stockholm, Sweden. Operations are conducted by Caltech’s Optical Observatory (COO), Caltech/IPAC, and the University of Washington at Seattle, USA.

SED Machine is based upon work supported by the National Science Foundation under Grant No. 1106171

The Gordon and Betty Moore Foundation, through both the Data-Driven Investigator Program and a dedicated grant, provided critical funding for SkyPortal.

APPENDIX A: VISION TRANSFORMERS FOR SPECTRA CLASSIFICATION

In this section, we present an alternative approach for spectral classification that leverages CNNs on image-based representations of spectra. Motivated by advances in vision transformer models (Sharma et al. 2025; Strano Moraes et al. 2025; Moreno-Cartagena et al. 2025), we developed a pipeline that renders one-dimensional flux–wavelength spectra as multi-channel images and processes them using a ConvNeXt-based architecture (Liu et al. 2022).

Our network is designed to handle multiband time-series data (e.g., g , r , and i bands) by converting each observation into an image-like format. These image representations are then passed through a ConvNeXt backbone adapted to accept three-channel input, allowing the model to capture both intra-band temporal features and cross-band correlations. The backbone is followed by a custom classification head consisting of fully connected layers, dropout regularization, and a softmax layer for multi-class prediction. Transfer learning is employed by initializing the ConvNeXt weights with pre-trained ImageNet parameters (Deng et al. 2009), followed by fine-tuning on our astrophysical dataset.

To generate the input images, we transform each one-dimensional flux–wavelength pair into a two-

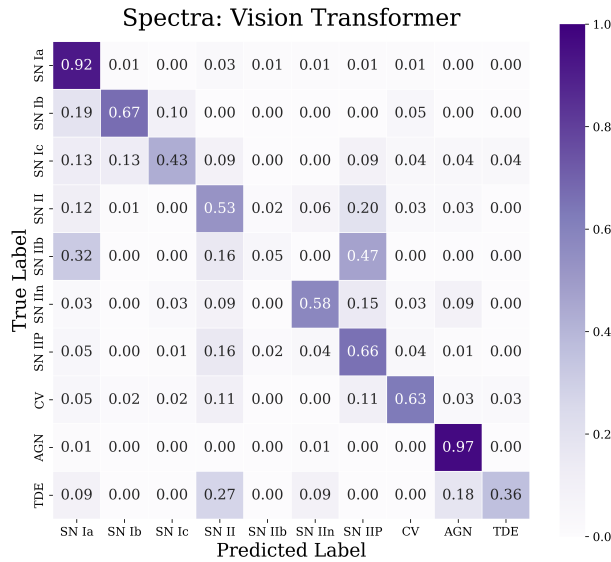


Figure 8. Confusion Matrix using vision transformers.

dimensional line plot using `matplotlib`. We avoid interpolation and resampling in order to retain the native spectral resolution and sampling characteristics of each instrument. All plot elements such as axes, tick marks, and grid lines were removed to eliminate visual bias, leaving only the flux curve on a white background.

To construct a richer, multi-channel input, we apply LOESS smoothing (Jacoby 2000) to each spectrum with different fractional span values. Specifically, we generate five separate plots: the original raw spectrum (unsmoothed), and four smoothed versions with span values of 0.01, 0.05, 0.1, and 0.2. Each curve is min–max normalized and rendered independently. These images are then stacked to form a $(3, H, W)$ tensor compatible with CNN-based architectures.

We experimented with multiple image resolutions (224×224 , 288×288 , and 384×384 pixels) and line widths (0.2, 1.0, and 2.0). The best classification performance was obtained using 288×288 resolution and a line width of 1.0. Moreover, we found that using only a subset of the smoothing channels—specifically, the raw curve along with LOESS-0.05 and LOESS-0.1—provided improved accuracy compared to using all five.

All rendered images are saved as NumPy arrays and are used directly as input to the classification model. The resulting confusion matrix is shown in Fig. 8. Although this approach yields reasonable performance, it exhibits notable confusion between certain classes, and the overall structure of the matrix is less diagonal compared to our final model presented in Sec. 3.

REFERENCES

- Abdurro’uf, Accetta, K., Aerts, C., et al. 2022, *ApJS*, 259, 35, doi: [10.3847/1538-4365/ac4414](https://doi.org/10.3847/1538-4365/ac4414)
- Akiba, T., Sano, S., Yanase, T., Ohta, T., & Koyama, M. 2019, *Optuna: A Next-generation Hyperparameter Optimization Framework*. <https://arxiv.org/abs/1907.10902>
- Aleo, P., Malanchev, K., Pruzhinskaya, M., et al. 2022, *New Astronomy*, 96, 101846, doi: <https://doi.org/10.1016/j.newast.2022.101846>
- Allam, Tarek, J., & McEwen, J. D. 2023, *RAS Techniques and Instruments*, 3, 209, doi: [10.1093/rasti/rzad046](https://doi.org/10.1093/rasti/rzad046)
- Amaro-Seoane, P., Andrews, J., Arca Sedda, M., et al. 2023, *Living Reviews in Relativity*, 26, doi: [10.1007/s41114-022-00041-y](https://doi.org/10.1007/s41114-022-00041-y)
- Andreoni, I., Coughlin, M. W., Kool, E. C., et al. 2021, *ApJ*, 918, 63, doi: [10.3847/1538-4357/ac0bc7](https://doi.org/10.3847/1538-4357/ac0bc7)
- Bellm, E. C., Kulkarni, S. R., Graham, M. J., et al. 2019, *PASP*, 131, 018002, doi: [10.1088/1538-3873/aaecbe](https://doi.org/10.1088/1538-3873/aaecbe)
- Blagorodnova, N., Neill, J. D., Walters, R., et al. 2018, *PASP*, 130, 035003, doi: [10.1088/1538-3873/aaa53f](https://doi.org/10.1088/1538-3873/aaa53f)
- Bloom, J. S., Richards, J. W., Nugent, P. E., et al. 2012, *PASP*, 124, 1175, doi: [10.1086/668468](https://doi.org/10.1086/668468)
- Boone, K. 2019, *AJ*, 158, 257, doi: [10.3847/1538-3881/ab5182](https://doi.org/10.3847/1538-3881/ab5182)
- Brink, H., Richards, J. W., Poznanski, D., et al. 2013, *MNRAS*, 435, 1047, doi: [10.1093/mnras/stt1306](https://doi.org/10.1093/mnras/stt1306)
- Cabrera-Vives, G., Moreno-Cartagena, D., Astorga, N., et al. 2024, *A&A*, 689, A289, doi: [10.1051/0004-6361/202449475](https://doi.org/10.1051/0004-6361/202449475)
- Carrasco-Davis, R., Reyes, E., Valenzuela, C., et al. 2021, *AJ*, 162, 231, doi: [10.3847/1538-3881/ac0ef1](https://doi.org/10.3847/1538-3881/ac0ef1)
- Carrasco Kind, M., & Brunner, R. J. 2013, *MNRAS*, 432, 1483, doi: [10.1093/mnras/stt574](https://doi.org/10.1093/mnras/stt574)
- Chaini, S., Mahabal, A., Kembhavi, A., & Bianco, F. 2024, *A&C*, 48, 100850, doi: [10.1016/j.ascom.2024.100850](https://doi.org/10.1016/j.ascom.2024.100850)
- Collaboration, T. L. S., Aasi, J., Abbott, B. P., et al. 2015, *Classical and Quantum Gravity*, 32, 074001, doi: [10.1088/0264-9381/32/7/074001](https://doi.org/10.1088/0264-9381/32/7/074001)
- Coughlin, M. W., Bloom, J. S., Nir, G., et al. 2023, *ApJS*, 267, 31, doi: [10.3847/1538-4365/acdee1](https://doi.org/10.3847/1538-4365/acdee1)
- Cui, Y., Jia, M., Lin, T.-Y., Song, Y., & Belongie, S. 2019, *Class-Balanced Loss Based on Effective Number of Samples*. <https://arxiv.org/abs/1901.05555>
- Dekany, R., Smith, R. M., Riddle, R., et al. 2020, *PASP*, 132, 038001, doi: [10.1088/1538-3873/ab4ca2](https://doi.org/10.1088/1538-3873/ab4ca2)

- Deng, J., Dong, W., Socher, R., et al. 2009, in 2009 IEEE Conference on Computer Vision and Pattern Recognition, 248–255, doi: [10.1109/CVPR.2009.5206848](https://doi.org/10.1109/CVPR.2009.5206848)
- DESI Collaboration, Adame, A. G., Aguilar, J., et al. 2024, *AJ*, 168, 58, doi: [10.3847/1538-3881/ad3217](https://doi.org/10.3847/1538-3881/ad3217)
- Devlin, J., Chang, M.-W., Lee, K., & Toutanova, K. 2018, arXiv e-prints, arXiv:1810.04805, doi: [10.48550/arXiv.1810.04805](https://doi.org/10.48550/arXiv.1810.04805)
- Dieleman, S., Willett, K. W., & Dambre, J. 2015, *MNRAS*, 450, 1441, doi: [10.1093/mnras/stv632](https://doi.org/10.1093/mnras/stv632)
- Drake, A. J., Djorgovski, S. G., Mahabal, A., et al. 2012, in IAU Symposium, Vol. 285, New Horizons in Time Domain Astronomy, ed. E. Griffin, R. Hanisch, & R. Seaman, 306–308, doi: [10.1017/S1743921312000889](https://doi.org/10.1017/S1743921312000889)
- Duev, D. A., Mahabal, A., Masci, F. J., et al. 2019, *MNRAS*, 489, 3582, doi: [10.1093/mnras/stz2357](https://doi.org/10.1093/mnras/stz2357)
- Duev, D. A., & van der Walt, S. J. 2021, Phenomenological classification of the Zwicky Transient Facility astronomical event alerts. <https://arxiv.org/abs/2111.12142>
- Eigen, D., Ranzato, M., & Sutskever, I. 2014, Learning Factored Representations in a Deep Mixture of Experts. <https://arxiv.org/abs/1312.4314>
- Fedus, W., Zoph, B., & Shazeer, N. 2022, Switch Transformers: Scaling to Trillion Parameter Models with Simple and Efficient Sparsity. <https://arxiv.org/abs/2101.03961>
- Fontinele Nunes, et al. 2025, in prep., AppleCiDER III: Photometry
- Förster, F., Cabrera-Vives, G., Castillo-Navarrete, E., et al. 2021, *AJ*, 161, 242, doi: [10.3847/1538-3881/abe9bc](https://doi.org/10.3847/1538-3881/abe9bc)
- Fremling, C., Miller, A. A., Sharma, Y., et al. 2020, *ApJ*, 895, 32, doi: [10.3847/1538-4357/ab8943](https://doi.org/10.3847/1538-4357/ab8943)
- Fremling, C., Hall, X. J., Coughlin, M. W., et al. 2021, *ApJL*, 917, L2, doi: [10.3847/2041-8213/ac116f](https://doi.org/10.3847/2041-8213/ac116f)
- Gehrels, N., Chincarini, G., Giommi, P., et al. 2004, *ApJ*, 611, 1005, doi: [10.1086/422091](https://doi.org/10.1086/422091)
- González-Bañuelos, M., Gutiérrez, C. P., Galbany, L., & González-Gaitán, S. 2025, Statistical Analysis of Early Spectra in Type II and IIb Supernovae. <https://arxiv.org/abs/2507.08731>
- Graham, M. J., Kulkarni, S. R., Bellm, E. C., et al. 2019, *PASP*, 131, 078001, doi: [10.1088/1538-3873/ab006c](https://doi.org/10.1088/1538-3873/ab006c)
- Gupta, R., Muthukrishna, D., & Lochner, M. 2024, *RAS Techniques and Instruments*, 4, doi: [10.1093/rasti/rzae054](https://doi.org/10.1093/rasti/rzae054)
- Hammerstein, E., van Velzen, S., Gezari, S., et al. 2023, *ApJ*, 942, 9, doi: [10.3847/1538-4357/aca283](https://doi.org/10.3847/1538-4357/aca283)
- He, K., Zhang, X., Ren, S., & Sun, J. 2016, *CVPR*. <https://arxiv.org/abs/1512.03385>
- Hendrycks, D., & Gimpel, K. 2016, arXiv preprint arXiv:1606.08415
- Hložek, R., Malz, A. I., Ponder, K. A., et al. 2023, *ApJS*, 267, 25, doi: [10.3847/1538-4365/accd6a](https://doi.org/10.3847/1538-4365/accd6a)
- Ho, A. Y. Q., Perley, D. A., Gal-Yam, A., et al. 2023, *ApJ*, 949, 120, doi: [10.3847/1538-4357/acc533](https://doi.org/10.3847/1538-4357/acc533)
- Hosseinzadeh, G., Dauphin, F., Villar, V. A., et al. 2020, *ApJ*, 905, 93, doi: [10.3847/1538-4357/abc42b](https://doi.org/10.3847/1538-4357/abc42b)
- Ishida, E. E. O., & de Souza, R. S. 2013, *MNRAS*, 430, 509, doi: [10.1093/mnras/sts650](https://doi.org/10.1093/mnras/sts650)
- Ivezić, Ž., Connolly, A., Vanderplas, J., & Gray, A. 2014, *Statistics, Data Mining and Machine Learning in Astronomy* (Princeton University Press)
- Ivezić, Ž., Kahn, S. M., Tyson, J. A., et al. 2019, *ApJ*, 873, 111, doi: [10.3847/1538-4357/ab042c](https://doi.org/10.3847/1538-4357/ab042c)
- Jacoby, W. G. 2000, *Electoral Studies*, 19, 577, doi: [https://doi.org/10.1016/S0261-3794\(99\)00028-1](https://doi.org/10.1016/S0261-3794(99)00028-1)
- Jamal, S., & Bloom, J. S. 2020, *ApJS*, 250, 30, doi: [10.3847/1538-4365/aba8ff](https://doi.org/10.3847/1538-4365/aba8ff)
- Karpenka, N. V., Feroz, F., & Hobson, M. P. 2012, *MNRAS*, 429, 1278. <https://api.semanticscholar.org/CorpusID:119203211>
- Kasliwal, M. M., Cannella, C., Bagdasaryan, A., et al. 2019, *PASP*, 131, 038003, doi: [10.1088/1538-3873/aafbc2](https://doi.org/10.1088/1538-3873/aafbc2)
- Kessler, R., Conley, A., Jha, S., & Kuhlmann, S. 2010, arXiv e-prints, arXiv:1001.5210, doi: [10.48550/arXiv.1001.5210](https://doi.org/10.48550/arXiv.1001.5210)
- Kessler, R., Narayan, G., Avelino, A., et al. 2019, *PASP*, 131, 094501, doi: [10.1088/1538-3873/ab26f1](https://doi.org/10.1088/1538-3873/ab26f1)
- Kiela, D., Bhooshan, S., Firooz, H., Perez, E., & Testuggine, D. 2020, Supervised Multimodal Bitransformers for Classifying Images and Text. <https://arxiv.org/abs/1909.02950>
- Kim, Y. L., Rigault, M., Neill, J. D., et al. 2022, *PASP*, 134, 024505, doi: [10.1088/1538-3873/ac50a0](https://doi.org/10.1088/1538-3873/ac50a0)
- Kulkarni, S. R., Harrison, F. A., Grefenstette, B. W., et al. 2023, Science with the Ultraviolet Explorer (UVEX). <https://arxiv.org/abs/2111.15608>
- Lanusse, F., Ma, Q., Li, N., et al. 2018, *MNRAS*, 473, 3895, doi: [10.1093/mnras/stx1665](https://doi.org/10.1093/mnras/stx1665)
- Law, N. M., Kulkarni, S. R., Dekany, R. G., et al. 2009, *PASP*, 121, 1395, doi: [10.1086/648598](https://doi.org/10.1086/648598)
- Lepikhin, D., Lee, H., Xu, Y., et al. 2020, GShard: Scaling Giant Models with Conditional Computation and Automatic Sharding. <https://arxiv.org/abs/2006.16668>
- Leung, H. W., & Bovy, J. 2023, *MNRAS*, 527, 1494, doi: [10.1093/mnras/stad3015](https://doi.org/10.1093/mnras/stad3015)
- Lin, T.-Y., Goyal, P., Girshick, R., He, K., & Dollár, P. 2018, Focal Loss for Dense Object Detection. <https://arxiv.org/abs/1708.02002>

- Liu, Z., Mao, H., Wu, C.-Y., et al. 2022, A ConvNet for the 2020s. <https://arxiv.org/abs/2201.03545>
- Lochner, M., McEwen, J. D., Peiris, H. V., Lahav, O., & Winter, M. K. 2016, *ApJS*, 225, 31, doi: [10.3847/0067-0049/225/2/31](https://doi.org/10.3847/0067-0049/225/2/31)
- Loshchilov, I., & Hutter, F. 2017, arXiv preprint arXiv:1608.03983. <https://arxiv.org/abs/1608.03983>
- . 2019, Decoupled Weight Decay Regularization. <https://arxiv.org/abs/1711.05101>
- Malz, A. I., Hložek, R., Allam, T., et al. 2019, *AJ*, 158, 171, doi: [10.3847/1538-3881/ab3a2f](https://doi.org/10.3847/1538-3881/ab3a2f)
- Masci, F. J., Laher, R. R., Rusholme, B., et al. 2019, *PASP*, 131, 018003, doi: [10.1088/1538-3873/aae8ac](https://doi.org/10.1088/1538-3873/aae8ac)
- Matheson, T., Stubens, C., Wolf, N., et al. 2021, *AJ*, 161, 107, doi: [10.3847/1538-3881/abd703](https://doi.org/10.3847/1538-3881/abd703)
- Mishra-Sharma, S., Song, Y., & Thaler, J. 2024, PAPERCLIP: Associating Astronomical Observations and Natural Language with Multi-Modal Models. <https://arxiv.org/abs/2403.08851>
- Moreno-Cartagena, D., Protopapas, P., Cabrera-Vives, G., et al. 2025, Leveraging Pre-Trained Visual Transformers for Multi-Band Photometric Light Curve Classification. <https://arxiv.org/abs/2502.20479>
- Mosby, G., Rauscher, B., Bennett, C., et al. 2020, *Journal of Astronomical Telescopes, Instruments, and Systems*, 6, 046001, doi: [10.1117/1.JATIS.6.4.046001](https://doi.org/10.1117/1.JATIS.6.4.046001)
- Mu, S., & Lin, S. 2025, A Comprehensive Survey of Mixture-of-Experts: Algorithms, Theory, and Applications. <https://arxiv.org/abs/2503.07137>
- Muthukrishna, D., Narayan, G., Mandel, K. S., Biswas, R., & Hložek, R. 2019, *PASP*, 131, 118002, doi: [10.1088/1538-3873/ab1609](https://doi.org/10.1088/1538-3873/ab1609)
- Muthukrishna, D., Parkinson, D., & Tucker, B. E. 2019, *ApJ*, 885, 85, doi: [10.3847/1538-4357/ab48f4](https://doi.org/10.3847/1538-4357/ab48f4)
- Möller, A., Peloton, J., Ishida, E. E. O., et al. 2020, *MNRAS*, 501, 3272, doi: [10.1093/mnras/staa3602](https://doi.org/10.1093/mnras/staa3602)
- Narayan, G., Zaidi, T., Soraisam, M. D., et al. 2018, *ApJS*, 236, 9, doi: [10.3847/1538-4365/aab781](https://doi.org/10.3847/1538-4365/aab781)
- Narihira, T., Alonsogarcia, J., Cardinaux, F., et al. 2021, Neural Network Libraries: A Deep Learning Framework Designed from Engineers' Perspectives. <https://arxiv.org/abs/2102.06725>
- Neira O., D., Estévez, P. A., & Förster, F. 2024, in 2024 International Joint Conference on Neural Networks (IJCNN), 1–9, doi: [10.1109/IJCNN60899.2024.10650191](https://doi.org/10.1109/IJCNN60899.2024.10650191)
- Noebauer, U. M., Kromer, M., Taubenberger, S., et al. 2017, *MNRAS*, 472, 2787, doi: [10.1093/mnras/stx2093](https://doi.org/10.1093/mnras/stx2093)
- Nun, I., Protopapas, P., Sim, B., et al. 2015, FATS: Feature Analysis for Time Series. <https://arxiv.org/abs/1506.00010>
- Parker, L., Lanusse, F., Golkar, S., et al. 2024, *MNRAS*, 531, 4990–5011, doi: [10.1093/mnras/stae1450](https://doi.org/10.1093/mnras/stae1450)
- Patterson, M. T., Bellm, E. C., Rusholme, B., et al. 2019, *PASP*, 131, 018001, doi: [10.1088/1538-3873/aae904](https://doi.org/10.1088/1538-3873/aae904)
- Perley, D. A., Fremling, C., Sollerman, J., et al. 2020, *ApJ*, 904, 35, doi: [10.3847/1538-4357/abbd98](https://doi.org/10.3847/1538-4357/abbd98)
- Pimentel, O., Estevez, P. A., & Forster, F. 2022, *AJ*, 165, 18, doi: [10.3847/1538-3881/ac9ab4](https://doi.org/10.3847/1538-3881/ac9ab4)
- Poudel, M., Sarode, R. P., Watanobe, Y., Mozgovoy, M., & Bhalla, S. 2022, *Applied Sciences*, 12, doi: [10.3390/app12126202](https://doi.org/10.3390/app12126202)
- Radford, A., Kim, J. W., Hallacy, C., et al. 2021, Learning Transferable Visual Models From Natural Language Supervision. <https://arxiv.org/abs/2103.00020>
- Rebbapragada, U., Protopapas, P., Brodley, C. E., & Alcock, C. 2008, *Machine Learning*, 74, 281–313, doi: [10.1007/s10994-008-5093-3](https://doi.org/10.1007/s10994-008-5093-3)
- Rehemtulla, N., Miller, A. A., Jegou Du Laz, T., et al. 2024, *ApJ*, 972, 7, doi: [10.3847/1538-4357/ad5666](https://doi.org/10.3847/1538-4357/ad5666)
- Rehemtulla, N., Jacobson-Galán, W. V., Singh, A., et al. 2025, *ApJ*, 985, 241, doi: [10.3847/1538-4357/adcf1e](https://doi.org/10.3847/1538-4357/adcf1e)
- Richards, J. W., Starr, D. L., Butler, N. R., et al. 2011, *ApJ*, 733, 10, doi: [10.1088/0004-637X/733/1/10](https://doi.org/10.1088/0004-637X/733/1/10)
- Rigault, M., Neill, J. D., Blagorodnova, N., et al. 2019, *A&A*, 627, A115, doi: [10.1051/0004-6361/201935344](https://doi.org/10.1051/0004-6361/201935344)
- Rizhko, M., & Bloom, J. S. 2025, *AJ*, 170, 28, doi: [10.3847/1538-3881/adcbad](https://doi.org/10.3847/1538-3881/adcbad)
- Rumelhart, D. E., Hinton, G. E., & Williams, R. J. 1986, *Nature*, 323, 533, doi: [10.1038/323533a0](https://doi.org/10.1038/323533a0)
- Sharma, Y., Mahabal, A. A., Sollerman, J., et al. 2025, *PASP*, 137, 034507, doi: [10.1088/1538-3873/adbf4b](https://doi.org/10.1088/1538-3873/adbf4b)
- Shazeer, N., Mirhoseini, A., Maziarz, K., et al. 2017, Outrageously Large Neural Networks: The Sparsely-Gated Mixture-of-Experts Layer. <https://arxiv.org/abs/1701.06538>
- Shvartzvald, Y., Waxman, E., Gal-Yam, A., et al. 2024, *ApJ*, 964, 74, doi: [10.3847/1538-4357/ad2704](https://doi.org/10.3847/1538-4357/ad2704)
- Stachie, C., Coughlin, M. W., Christensen, N., & Muthukrishna, D. 2020, *MNRAS*, 497, 1320, doi: [10.1093/mnras/staa1776](https://doi.org/10.1093/mnras/staa1776)
- Strano Moraes, L. F., Becker, I., Protopapas, P., & Cabrera-Vives, G. 2025, arXiv e-prints, arXiv:2506.00294, doi: [10.48550/arXiv.2506.00294](https://doi.org/10.48550/arXiv.2506.00294)
- Sánchez-Sáez, P., Reyes, I., Valenzuela, C., et al. 2021, *AJ*, 161, 141, doi: [10.3847/1538-3881/abd5c1](https://doi.org/10.3847/1538-3881/abd5c1)
- Tarvainen, A., & Valpola, H. 2018, Mean teachers are better role models: Weight-averaged consistency targets improve semi-supervised deep learning results. <https://arxiv.org/abs/1703.01780>

- The PLAsTiCC team, Allam, Jr., T., Bahmanyar, A., et al. 2018, arXiv e-prints, arXiv:1810.00001, doi: [10.48550/arXiv.1810.00001](https://doi.org/10.48550/arXiv.1810.00001)
- Tonry, J. L., Denneau, L., Heinze, A. N., et al. 2018, PASP, 130, 064505, doi: [10.1088/1538-3873/aabadf](https://doi.org/10.1088/1538-3873/aabadf)
- van der Walt, S. J., Crellin-Quick, A., & Bloom, J. S. 2019, Journal of Open Source Software, 4, 1247, doi: [10.21105/joss.01247](https://doi.org/10.21105/joss.01247)
- Vanderplas, J., Connolly, A., Ivezić, Ž., & Gray, A. 2012, in Conference on Intelligent Data Understanding (CIDU), 47–54, doi: [10.1109/CIDU.2012.6382200](https://doi.org/10.1109/CIDU.2012.6382200)
- Varughese, M. M., von Sachs, R., Stephanou, M., & Bassett, B. A. 2015, MNRAS, 453, 2848, doi: [10.1093/mnras/stv1816](https://doi.org/10.1093/mnras/stv1816)
- Villar, V. A., Cranmer, M., Berger, E., et al. 2021, ApJS, 255, 24, doi: [10.3847/1538-4365/ac0893](https://doi.org/10.3847/1538-4365/ac0893)
- Villar, V. A., Hosseinzadeh, G., Berger, E., et al. 2020, ApJ, 905, 94, doi: [10.3847/1538-4357/abc6fd](https://doi.org/10.3847/1538-4357/abc6fd)
- Villar, V. A., Berger, E., Miller, G., et al. 2019, ApJ, 884, 83, doi: [10.3847/1538-4357/ab418c](https://doi.org/10.3847/1538-4357/ab418c)
- Wu, Y., Tao, Y., Fan, D., Cui, C., & Zhang, Y. 2024, MNRAS, 527, 1163, doi: [10.1093/mnras/stad2913](https://doi.org/10.1093/mnras/stad2913)
- Xu, et al. 2025, in prep., AppleCiDEr II: SpectraNet – A Multi-Scale 1D Convolutional Architecture for Supernova Spectral Classification
- Yaron, O., & Gal-Yam, A. 2012, PASP, 124, 668–681, doi: [10.1086/666656](https://doi.org/10.1086/666656)
- Yuan, W., Zhang, C., Chen, Y., & Ling, Z. 2022, The Einstein Probe Mission (Springer Nature Singapore), 1–30, doi: [10.1007/978-981-16-4544-0_151-1](https://doi.org/10.1007/978-981-16-4544-0_151-1)
- Zaman, S., Smith, M. J., Khetarpal, P., et al. 2025, AstroLLaVA: towards the unification of astronomical data and natural language. <https://arxiv.org/abs/2504.08583>
- Zerveas, G., Jayaraman, S., Patel, D., Bhamidipaty, A., & Eickhoff, C. 2020, arXiv e-prints, arXiv:2010.02803, doi: [10.48550/arXiv.2010.02803](https://doi.org/10.48550/arXiv.2010.02803)
- Zhang, G., Helfer, T., Gagliano, A. T., Mishra-Sharma, S., & Ashley Villar, V. 2024, Machine Learning: Science and Technology, 5, 045069, doi: [10.1088/2632-2153/ad990d](https://doi.org/10.1088/2632-2153/ad990d)
- Zhang, Y., & Zhao, Y. 2015, Data Science Journal, doi: [10.5334/dsj-2015-011](https://doi.org/10.5334/dsj-2015-011)
- Zhou, H., Zhang, S., Peng, J., et al. 2020, arXiv e-prints, arXiv:2012.07436, doi: [10.48550/arXiv.2012.07436](https://doi.org/10.48550/arXiv.2012.07436)
- Zuo, X., Tao, Y., Huang, Y., et al. 2025, FALCO: a Foundation model of Astronomical Light Curves for time domain astronomy. <https://arxiv.org/abs/2504.20290>